SCIENTIFIC REPORTS
nature research

Check for updates

OPEN

Interface Engineered Binary Platinum Free Alloy-based Counter Electrodes with Improved Performance in Dye-Sensitized Solar Cells

Wen-Wu Liu[1,2]✉, Wei Jiang[1,2], Yu-Cheng Liu[1,2], Wen-Jun Niu[1,2], Mao-Cheng Liu[1,2], Ling-Bin Kong[1,2], Ling Lee[3,6], Zhiming M. Wang[6] & Yu-Lun Chueh[3,4,5]✉

The high cost and platinum dissolution issues of counter electrodes (CEs) are two core problems for the development of dye-sensitized solar cells (DSSCs). In this work, different CEs based on binary alloy $Ru_{81.09}Co_{18.91}$, $Ru_{80.55}Se_{19.45}$ and $Co_{20.85}Se_{79.15}$ nanostructures for DSSCs were successfully synthesized and investigated by a facile and environmentally friendly approach. Here, we found that the $Co_{20.85}Se_{79.15}$ alloy CE-based device yields the higher photoelectric conversion efficiency of 7.08% compared with that (5.80%) of the DSSC using a pure Pt CE because of the larger number of active sites with improved charge transferability and reduced interface resistance by matching work function with the I_3^-/I^- redox electrolyte. The inexpensive synthesis method, cost-effectiveness and superior catalytic activity of the $Co_{20.85}Se_{79.15}$ alloy may open up a new avenue for the development of CEs for DSSCs in the near future.

Advanced electrocatalysts play a crucial role in fuel cells, air batteries and dye-sensitized solar cells (DSSCs)[1–3]. Platinum (Pt) metal is commonly considered a good electrocatalyst due to its superior electrocatalytic activity in the I_3^- reduction reaction at the electrolyte/counter electrode (CE) interface, good electrical conductivity, and high sunlight reflection ability in DSSCs[4]. However, the Pt metal suffers from drawbacks, such as expensive cost and unstable stability because of a dissolution reaction exposed to the I_3^-/I^- redox electrolyte. Particularly, the dissolution loss of the Pt metal may reduce the long-term stability of the photovoltaic efficiency of DSSCs. It is very important that developing a novel type of electrocatalyst has been one of the key objectives in studies focused on DSSCs. However, the most current research aimed at enhancing the electrocatalytic performance is still limited to the partial substitution of Pt with conductive polymers or carbon-based materials, or to the complete substitution of Pt with metal carbides, oxides, sulfides, and selenides[5–7]. The structure of these CEs would also be destroyed by the I_3^-/I^- based electrolyte under long-term electrochemical cycling[8].

Consequently, metal alloy-based electrocatalysts have attracted considerable attention due to their outstanding properties. Generally, these alloys involve the combination of Pt meal with transition metal elements denoted as PtM_x compounds (M = Fe, Co, Ni, Pd, Ru, Cu, etc.)[9–11]. Work function calculation and experimental analyses indicate that binary PtM_x alloys have better electrocatalytic properties toward I_3^- reduction[11–13]. It has been reported that the decreased resistance at the PtM_x/electrolyte interface and the competitive dissolution reaction between Pt and the transition metal effectively contribute to the enhanced electrocatalytic ability and stability of CEs[14,15]. Different lattice parameters in the structure of PtM_x alloys would result in ligand and strain effects[16],

[1]State Key Laboratory of Advanced Processing and Recycling of Nonferrous Metals, Lanzhou University of Technology, Lanzhou, 730050, PR China. [2]College of Materials Science and Engineering, Lanzhou University of Technology, Lanzhou, 730050, PR China. [3]Department of Materials Science and Engineering, National Tsing Hua University, Hsinchu, 30013, Taiwan. [4]Frontier Research Center on Fundamental and Applied Sciences of Matters, National Tsing Hua University, Hsinchu, 30013, Taiwan. [5]Department of Physics, National Sun Yat-Sen University, Kaohsiung, 80424, Taiwan. [6]Institute of Fundamental and Frontier Sciences, University of Electronic Science and Technology of China, Chengdu, P. R. China. ✉e-mail: lww06080428@163.com; ylchueh@mx.nthu.edu.tw

thereby generating very large numbers of active sites for the reduction reaction of I_3^- ions. Nevertheless, the work functions of some bimetallic PtM_x alloys, such as PtCo, PtRu, or PtPd do not match the potential of the I_3^-/I^--based electrolyte, leading to unsatisfactory electrocatalytic activity and electron transport[17–19]. Meanwhile, the high cost of Pt metal is still a crucial obstacle for the further development of DSSCs.

In recent years, perovskite solar cells have attracted considerable attention worldwide with a corresponding gradual decrease in the number of studies focused on bimetallic Pt-free alloy electrocatalysts for DSSCs. From this perspective, the development of Pt-free polymetallic alloys has become a very important subject in the electrocatalysis field. Yin *et al*. synthesized a novel N-doped-carbon coated $CoSe_2$ on a 3D carbon cloth as a photocathode for DSSCs, which exhibited a good photoelectric efficiency (8.40%) and cycle stability[20]. A carbon shell coated $CoSe_2$ nanoparticles catalyst-based DSSC was also reported, which gives the good conversion efficiency of 7.54%[21]. Wang *et al*. reported a $Co_{0.85}Se$ and $Ni_{0.85}Se$ CE -based DSSCs with high efficiency of 9.40 and 8.32%, respectively, which were synthesized by *in situ* growth using a hydrothermal method[22]. These results indicate that transition metal selenides have superior catalytic activities than the pristine Pt CE for DSSCs. In this case, for the purpose of reducing the fabrication cost and improving their electrocatalytic activity and stability in DSSCs, the Pt-free bimetallic alloys including RuCo, RuSe and CoSe -based CEs were synthesized by a simple electrodeposition approach. The exact compositions of $Ru_{81.09}Co_{18.91}$, $Ru_{80.55}Se_{19.45}$ and $Co_{20.85}Se_{79.15}$ can be confirmed by Energy Dispersive Spectrometer (EDS) and X-ray photoelectron spectroscopy (XPS) characterization. As a result, the power conversion efficiency of $Co_{20.85}Se_{79.15}$ CE-based DSSCs reached 7.08%, compared with the 5.80% value of pure Pt CE-based DSSCs. The improved catalytic performance can be attributed to the matching work function, a large number of active sites and reduced interface resistance.

Results and discussion

High-magnification FESEM images of various alloy CEs electrodeposited on the surface of the FTO glass are shown in Fig. 1(a–f). The $Ru_{81.09}Co_{18.91}$, $Ru_{80.55}Se_{19.45}$, and $Co_{20.85}Se_{79.15}$ alloy CEs exhibited uniformly distributed surface morphologies compared to those of pure metal (Ru, Se, and Co) CEs. The alloy CEs showed a smaller average particle diameter and an almost homogeneous distribution (Fig. 1(a–c)), whereas a larger grain size and non-uniform surface appearance were observed for the pure metal CEs (Fig. 1(d–f)). XRD results of $Co_{20.85}Se_{79.15}$ alloy was characterized as shown in Figure S1, the peaks at 37.62°, 51.57° match well with (211) and (311) crystalline faces of $CoSe_2$ (JCPDS PDF#09-0234), respectively. The peak at 51.52° can be well indexed to (200) face of Co (JCPDS PDF#15-0806). The peak at 33.33°, 61.57° can be well indexed to (101) and (103) face of Se (JCPDS PDF#27-0601). In order to confirm the composition of the metal alloys, the CEs were analyzed by the EDS method as shown in Figure S2 and the corresponding quantitatively compositional results were shown in Table 1, for which the atomic molar ratios of the alloys were found to be 1:0.4, 1:0.3, and 1.2:3.4, respectively. Therefore, the chemical compositions of the RuCo, RuSe and CoSe alloy CEs could be expressed as $Ru_{81.09}Co_{18.91}$, $Ru_{80.55}Se_{19.45}$ and $Co_{20.85}Se_{79.15}$, respectively.

The X-ray photoelectron spectroscopy (XPS) spectra were also utilized to characterize the formation of different alloys as shown in Fig. 2. From Fig. 2(a,d,g), the Ru and Co, Ru and Se, Co and Se elements can be identified to be $Ru_{81.09}Co_{18.91}$, $Ru_{80.55}Se_{19.45}$ and $Co_{20.85}Se_{79.15}$, respectively. As can be shown in Fig. 2(b), the two peaks located at 280.5 and 281.2 eV were attributed to the bonding results of Ru-O and Ru-Ru. The Co 2p spectrum in Fig. 2(c) can be distributed into shakeup satellites (Sat.) and spin-orbit doublets. The first double peak at 780.7 and 796.6 eV, and the second speaks at 782.0 and 797.8 eV belong to Co^{2+} and Co^{3+}, respectively[21–23]. The shakeup double peaks indicated the formation of the Co-Co bond[21–23]. Fig. 2(e) exhibits the Ru 3d spectrum of $Ru_{80.55}Se_{19.45}$ alloy while two peaks located at 280.3 and 281.1 eV were assigned to the bonding results of Ru-Se and Ru-Ru. The doublet peaks at 54.5 and 55.5 eV in Fig. 2(f) can be ascribed to the bonding results of Ru-Se and Se-Se[21,24]. Fig. 2(h) shows the Co 2p spectrum of $Co_{20.85}Se_{79.15}$ alloy. Similarly, the first doublet peaks at 780.9 and 796.5 eV, and the second speaks at 783.2 and 798.6 eV suggest the bonding results of Se-Co-Se and Co-O, respectively[21–23,25]. From Fig. 2(i), the two peaks at 53.8 and 54.6 eV were related to the bonding results of Co-Se and Se-Se, respectively[21,24]. The results indicated that the $Co_{20.85}Se_{79.15}$ alloy can be composed of $CoSe_2$, Co_2O_3, Co and Se. It is believed that the alloy CEs can provide a higher number of active sites for the adsorption of I_3^- ions and their reduction reaction ($I_3^- + 2e^- = 3I^-$), thereby accelerating the electrocatalytic reaction on the electrolyte/CEs interface as well as the transport of electrons. The smaller crystalline size of the alloy CEs may be explained in terms of the crystal growth occurring during the electrodeposition process. The multiple crystal nuclei on the alloy surface would contribute to the formation of smaller nanocrystals[26].

Figure 3(a,b) display the photocurrent density-voltage plots of different CE-based DSSCs with and without sunlight illumination, respectively. Figure 3(c) shows the corresponding device configuration of the binary alloy CEs in DSSCs. The photoelectric parameters of the DSSCs are also shown in Table 2. Clearly, the transition metal alloys ($Ru_{81.09}Co_{18.91}$, $Ru_{80.55}Se_{19.45}$ and $Co_{20.85}Se_{79.15}$) considerably enhance the photoelectric conversion efficiency (PCE) of the DSSCs compared with that of pure metals (Ru, Se and Co). Improved PCEs of 4.57, 3.82 and 7.08% were achieved for the $Ru_{81.09}Co_{18.91}$, $Ru_{80.55}Se_{19.45}$ and $Co_{20.85}Se_{79.15}$ alloy CE-based DSSCs, respectively. In particular, the optimal DSSC based on $Co_{20.85}Se_{79.15}$ CE yielded a significantly improved photovoltaic performance ($J_{sc} = 15.91\ mA\ cm^{-2}$, $V_{oc} = 0.71$, $FF = 0.62$ and $PCE = 7.08\%$) compared with those of the Pt-based DSSCs ($J_{sc} = 14.72\ mA\ cm^{-2}$, $V_{oc} = 0.69$, $FF = 0.57$ and $PCE = 5.80\%$). Figure S3 exhibits the box charts, showing the statistical distribution of J_{sc}, V_{oc}, *FF* and *PCE* of the pristine Pt and $Co_{20.85}Se_{79.15}$ CE based DSSCs, respectively. The average *FF* (0.59) of $Co_{20.85}Se_{79.15}$ CE based devices is larger than that (0.55) of the pristine Pt-based DSSCs (Figure S3-c). Meanwhile, the average *PCE* of $Co_{20.85}Se_{79.15}$ based DSSCs is enhanced from 5.66% for the pristine Pt-based counterparts to 6.85% (Figure S3-d) as a result of the increased J_{sc} and *FF*. The improved performance of the DSSCs can be attributed to the matched work function, reduced interface resistance and smaller crystal particles of $Co_{20.85}Se_{79.15}$, which offers a much higher number of active sites for adsorption and reduction of I_3^- ions. Therefore, the reduced electron-transfer resistance between the electrolyte and the $Co_{20.85}Se_{79.15}$ CE can

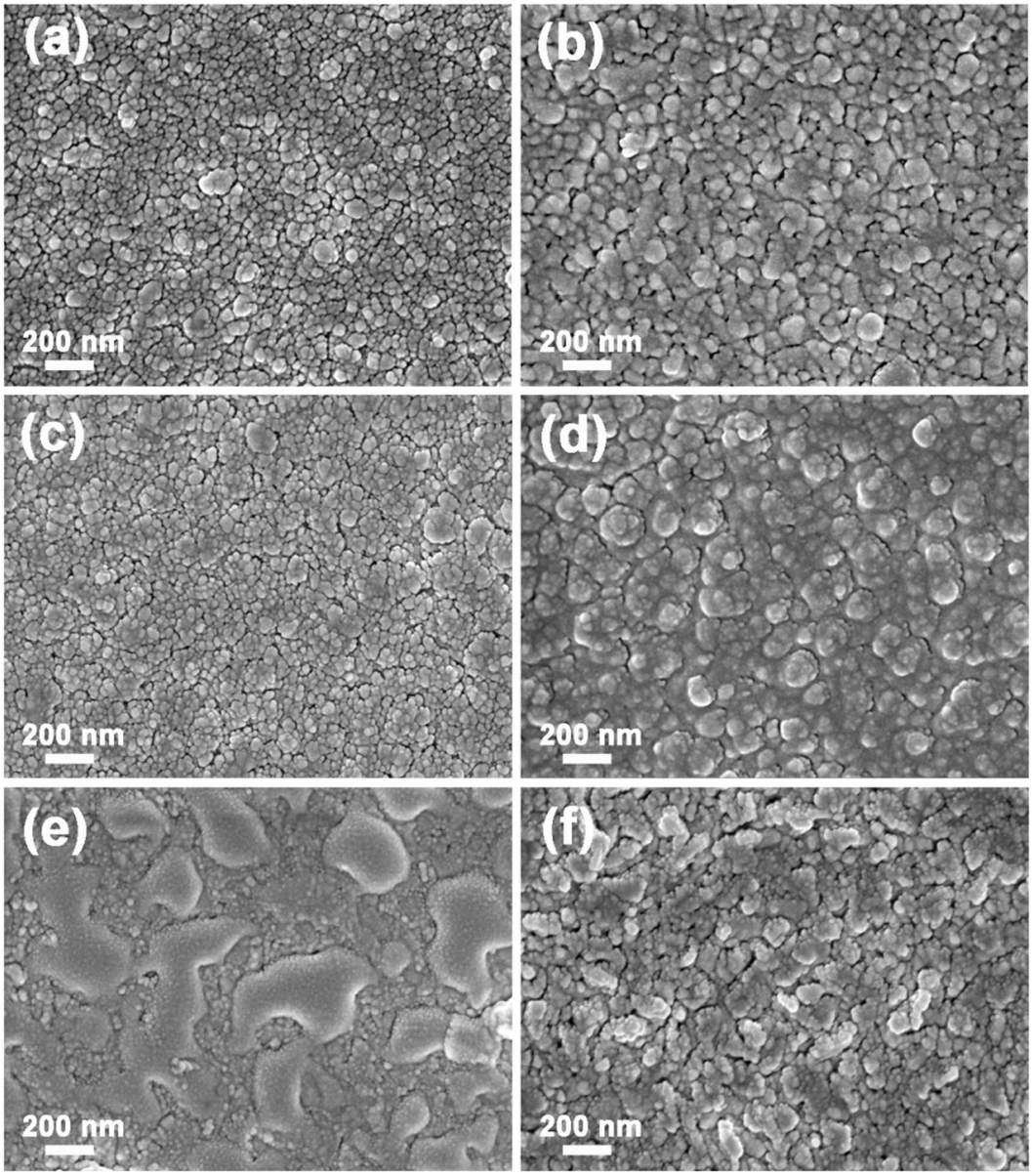

Figure 1. Top-view FESEM images of different alloys and pristine metal CEs at high magnification. (**a**) $Ru_{81.09}Co_{18.91}$, (**b**) $Ru_{80.55}Se_{19.45}$, (**c**) $Co_{20.85}Se_{79.15}$, (**d**) Ru, (**e**) Se, (**f**) Co.

RuCo		RuSe		CoSe	
Element	Atomic ratio	Element	Atomic ratio	Element	Atomic ratio
Ru	1.0	Ru	1.0	Co	1.2
Co	0.4	Se	0.3	Se	3.4

Table 1. The quantitative EDS results of corresponding binary alloys CEs.

efficiently accelerate the reduction reaction and the electron transport, resulting in the enhanced efficiency of the DSSCs. Furthermore, a dark current, the characteristic feature associated with recombination reactions between photogenerated electrons at the conduction band of TiO_2 and the electrolyte (I_3^-), was investigated as shown in Fig. 3(b). Clearly, the $Co_{20.85}Se_{79.15}$ alloy exhibited the smallest dark current density compared to that of pristine Pt, other alloys ($Ru_{81.09}Co_{18.91}$ and $Ru_{80.55}Se_{19.45}$) and pure metals (Ru, Se and Co), demonstrating suppression of the electron-loss reaction. The result can be explained by the fact that the $Co_{20.85}Se_{79.15}$ alloy can accelerate the kinetics of the reduction reaction, namely, $I_3^- + 2e^- = 3I^-$ and the regeneration rate of dye molecules. Therefore, the $Co_{20.85}Se_{79.15}$ alloy possesses advantages, such as a higher number of active sites, matched energy levels and

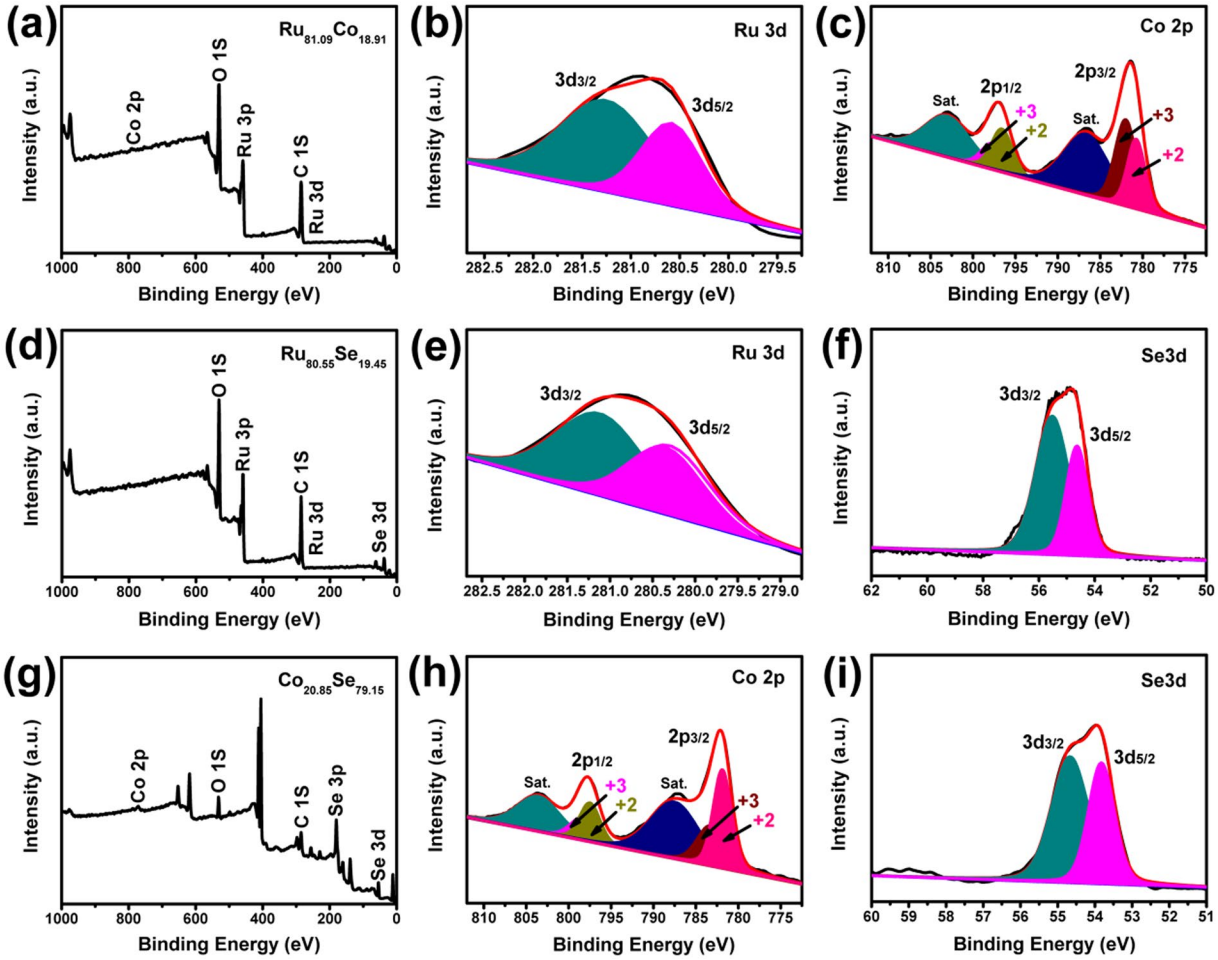

Figure 2. XPS spectra of Pt-free alloys (**a-c**) $Ru_{81.09}Co_{18.91}$, (**d-f**) $Ru_{80.55}Se_{19.45}$, (**g-i**) $Co_{20.85}Se_{79.15}$ CEs.

reduced interface resistance, resulting in a fast electrolyte (I_3^-) reduction at the electrolyte/CE interface instead of the recombination with electrons originated from the TiO_2 conduction band.

The electrocatalytic activities of the alloy CEs towards I_3^- reduction were also investigated by electrochemical methods as shown in Fig. 4. Figure 4(a) shows cyclic voltammogram (CV) of the different CEs where two couples of redox peaks can be seen in the CV plots. The redox peaks on the left side of the figures correspond to the $I_3^- \rightarrow I^-$ process (red_1: $I_3^- + 2e^- = 3I^-$, ox_1: $3I^- - 2e^- = I_3^-$) while the ones on the right correspond to the $I_2 \rightarrow I_3^-$ process (red_2: $3I_2 + 2e^- = 2I_3^-$, ox_2: $2I_3^- - 2e^- = 3I_2$)[26]. Since the $I_3^- \rightarrow I^-$ reduction process is the dominating reaction in I_3^-/I^--based electrolyte systems, we mainly focus on the left redox peaks. The plot shows that the redox peaks of alloy CEs are much stronger than those of the pristine metals (Ru, Se and Co), suggesting that the alloy CEs have a superior catalytic activity toward I_3^- reduction. Table 3 shows electrochemical parameters obtained from CV plots and EIS at different CEs where the J_{red1} and E_{red1} represent the peak current density and potential of reduction reaction (red_1), respectively. Because J_{red1} is a key parameter for estimating the electrocatalytic activity of CEs[27], clearly, the J_{red1} decreases in the order $Co_{20.85}Se_{79.15} > Pt > Ru_{81.09}Co_{18.91} > Ru_{80.55}Se_{19.45} > Ru > Se > Co$, highlighting the superior catalytic properties of the $Co_{20.85}Se_{79.15}$ alloy. Moreover, the Randles-Sevcik theory was used to investigate the ion diffusion at the electrolyte/CE interface. The electron diffusion coefficient, D_n, was determined from the equation $J_{red1} = kn^{1.5}AD_n^{0.5}C_0\nu^{0.5}$ where C_0 is the I_3^-/I^- ion concentration, ν is the scan rate, A is the active area of the CEs, n is the number of electrons involved in the reduction process and K is a constant[28,29]. As a result, the calculated D_n values of $Ru_{81.09}Co_{18.91}$, $Ru_{80.55}Se_{19.45}$, $Co_{20.85}Se_{79.15}$, Ru, Se, Co and Pt were 2.47×10^{-5}, 2.22×10^{-5}, 3.67×10^{-5}, 0.37×10^{-5}, 0.06×10^{-5}, 0.03×10^{-5} and 3.05×10^{-5}, respectively. The improved D_n of the $Co_{20.85}Se_{79.15}$ alloy denotes the faster diffusion kinetics of I_3^- ions between electrolyte and CEs. The higher number of active sites and the ligand effect between Co and Se are also expected to contribute the enhanced catalytic properties of the corresponding alloy CEs. Figure 4(b) shows the relationship between the square root of the scan rates and the peak current density where CV plots obtained for the CEs at different scan rates are shown in Figure S4. Obviously, the peak current density of reduction and oxidation increased almost linearly with the scan rate, indicating that the electrochemical reaction is controlled by the diffusion behavior of I_3^- ions at the electrolyte/CE interface[30]. In order to examine the internal electron transfer kinetics at the electrolyte/CE interface, Nyquist EIS curves of symmetrical devices, consisting of two identical CEs and the electrolyte, were measured and displayed in Fig. 4(c,d), respectively. The charge-transfer resistance (R_{ct}) between electrolyte and CEs determined by

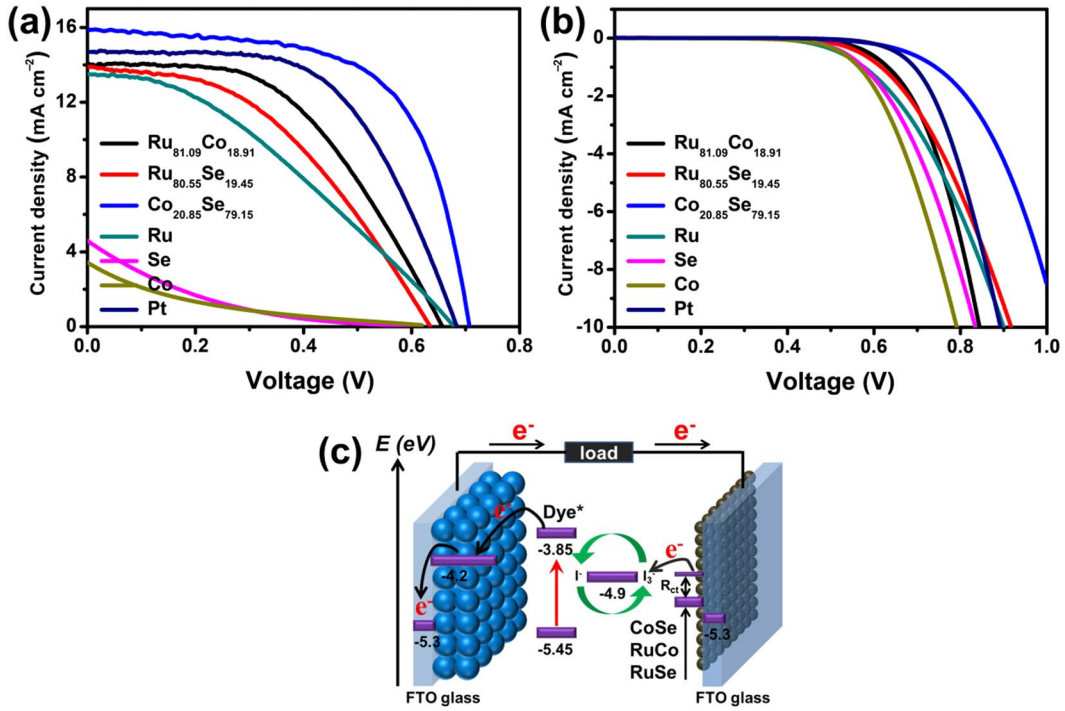

Figure 3. Photocurrent density-voltage curves of various CEs based DSSCs (**a**) with sunlight and (**b**) at dark condition, (**c**) device configuration of the alloy CEs supported DSSC.

CEs	J_{sc} (mA cm^{-2})	V_{oc} (V)	*FF*	η (%)
$Ru_{81.09}Co_{18.91}$	14.07	0.66	0.49	4.57
$Ru_{80.55}Se_{19.45}$	13.90	0.64	0.43	3.82
$Co_{20.85}Se_{79.15}$	15.91	0.71	0.62	7.08
Ru	13.50	0.67	0.36	3.22
Se	4.59	0.62	0.12	0.34
Co	3.43	0.62	0.13	0.27
Pt	14.72	0.69	0.57	5.80

Table 2. Photovoltaic parameters of different CEs based DSSCs under AM 1.5 G sunlight (100 mW cm^{-2}) illumination. J_{sc}: Short-circuit current density, V_{oc}: Open-circuit voltage, *FF*: fill factor, η**:** Photo-electric conversion efficiency.

fitting the Nyquist plots increase in the following order of $Co_{20.85}Se_{79.15}$ < Pt < $Ru_{81.09}Co_{18.91}$ < $Ru_{80.55}Se_{19.45}$ < Ru <Se <Co where the equivalent circuit is displayed in Fig. 3(c). A smaller R_{ct} denotes a rapid electron transport kinetics at the electrolyte/CE interface (Table 3). Therefore, the catalytic reactions are effectively accelerated by the $Co_{20.85}Se_{79.15}$ alloy CEs and can be further confirmed by examining the interfacial electron lifetimes ($\tau_e = 0.5\pi f_{peak}$ where f_{peak} represents the peak frequency in the Bode plots displayed in Fig. 4e) as shown in Fig. 4(e) and Table 4 shows electrochemical parameters obtained from the EIS and Tafel polarization plots based on CE/electrolyte/CE structures[31]. The calculated lifetimes varied in the following order of $Co_{20.85}Se_{79.15}$ (15.91 μs) <Pt (59.28 μs) <$Ru_{81.09}Co_{18.91}$ (93.18 μs) <$Ru_{80.55}Se_{19.45}$ (518.10 μs) <Ru (2334.83 μs) <Se (2833.37 μs) <Co (3431.80 μs), respectively. Lower τ_e values indicate the faster reduction kinetics of I_3^- ions, yielding the improved electrocatalytic ability of the CEs. These results are in good agreement with the CV plots. Based on the Tafel polarization plots in Fig. 4(f), the exchange and diffusion-limited current densities (J_0 and J_{lim}, respectively) can be calculated from the equations[9] $J_0 = RT/nFR_{ct}$ and $J_{lim} = 2nFCD_n/l$, respectively (Table 4). The obtained J_0 and J_{lim} values also decreased in the order $Co_{20.85}Se_{79.15}$ > Pt> $Ru_{81.09}Co_{18.91}$ > $Ru_{80.55}Se_{19.45}$ > Ru> Se> Co, in good agreement with the CV and EIS results. Therefore, the present results allow us to conclude that binary $Co_{20.85}Se_{79.15}$ alloy CEs possess superior catalytic abilities compared with alloy and pure Pt CEs. Furthermore, 100 cycles of CV plots from $Co_{20.85}Se_{79.15}$ and Pt CE in I_3^-/I^- redox electrolyte were used to evaluate the electrochemical stability as shown in Fig. 5, for which the peak current density J_{red1} of $Co_{20.85}Se_{79.15}$ CE can retain 96% of its initial value while the J_{red1} of Pt CE decreases to 83% of initial value. The results indicate that the alloy $Co_{20.85}Se_{79.15}$ CE possesses superior electrochemical stability in the I_3^-/I^- supported electrolyte.

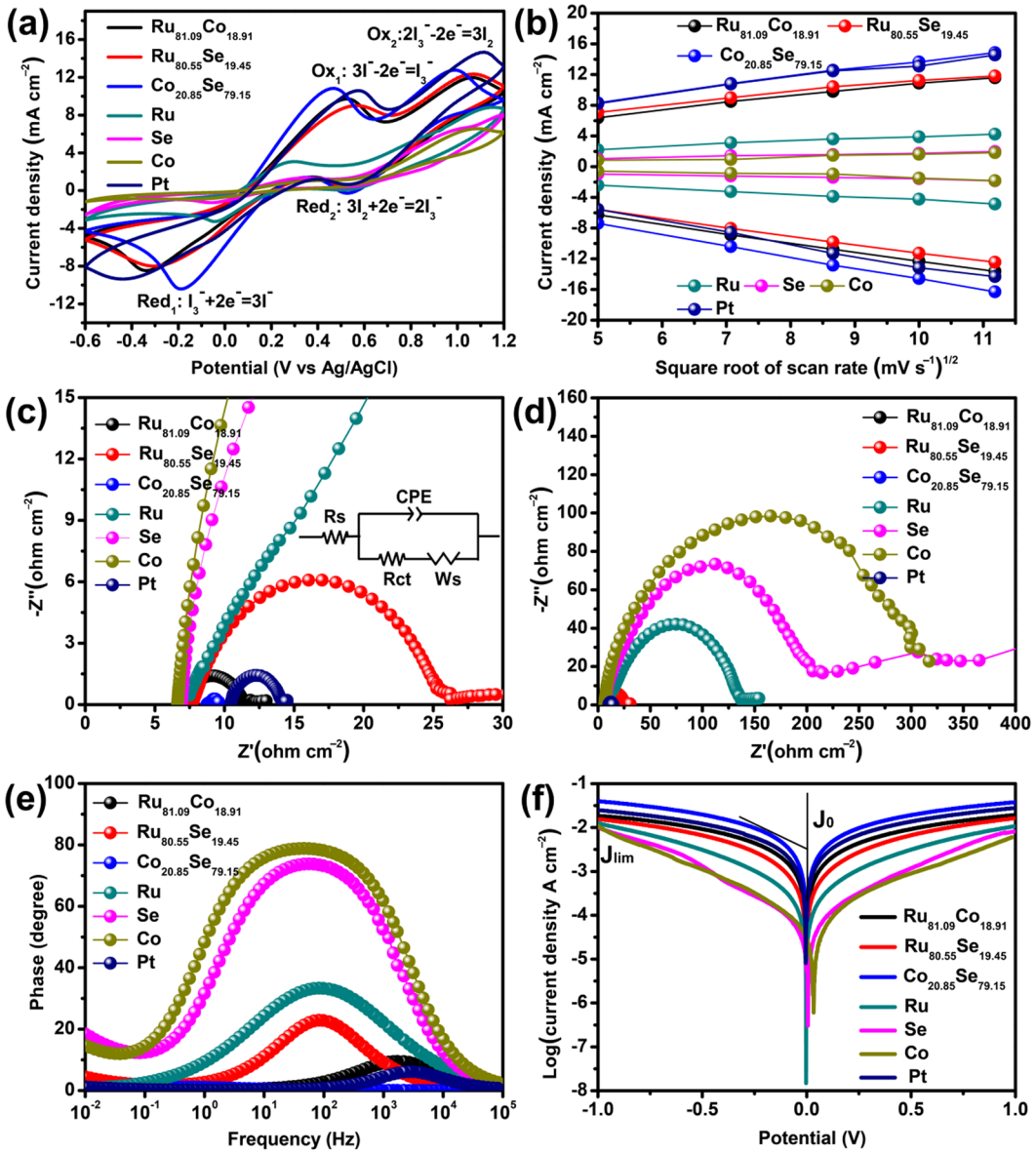

Figure 4. (**a**) CV plots of different CEs based cells in the N_2 cleaned I_3^-/I^- redox couple electrolyte measured at a scan rate of 50 mV s^{-1}. (**b**) Relationship between square root of scan rates and peak current density. (**c-d**) Nyquist EIS curves, (**e**) Bode plots and (**f**) Tafel polarization plots of symmetric dummy devices (CE/electrolyte/CE).

CEs	J_{red1} (mA cm^{-2})	E_{red1} (V)	D_n (cm^2 s^{-1})	R_{ct} (Ω cm^{-2})
$Ru_{81.09}Co_{18.91}$	–8.475	–0.338	2.47×10^{-5}	4.32
$Ru_{80.55}Se_{19.45}$	–8.033	–0.292	2.22×10^{-5}	18.27
$Co_{20.85}Se_{79.15}$	–10.320	–0.191	3.67×10^{-5}	1.26
Ru	–3.291	–0.041	0.37×10^{-5}	124.86
Se	–1.267	–0.059	0.06×10^{-5}	198.80
Co	–0.873	–0.130	0.03×10^{-5}	291.46
Pt	–9.406	–0.425	3.05×10^{-5}	3.45

Table 3. Electrochemical parameters obtained from CV plots and EIS based on CE/electrolyte/CE devices of different CEs.

In order to further investigate the internal mechanism of the CEs, the work functions of the different CEs were determined by SKPM using a gold probe (5.1 eV) as a standard reference, and are shown in Fig. 6. According to the SKPM analysis, the work functions of $Ru_{81.09}Co_{18.91}$, $Ru_{80.55}Se_{19.45}$, $Co_{20.85}Se_{79.15}$, Ru, Se and Co are –5.12,

CEs	Bode parameters f_{peak} (Hz)	τ_e (μs)	Tafel parameters J_0 (mA cm^{-2})	J_{lim} (mA cm^{-2})
$Ru_{81.09}Co_{18.91}$	1709	93.18	2.97	20.89
$Ru_{80.55}Se_{19.45}$	82.5	518.10	0.70	19.50
$Co_{20.85}Se_{79.15}$	10010	15.91	10.19	31.63
Ru	68.2	2334.83	0.36	12.60
Se	56.2	2833.37	0.28	10.23
Co	46.4	3431.80	0.26	10.96
Pt	2686	59.28	3.72	25.12

Table 4. Electrochemical parameters obtained from the EIS and Tafel polarization plots based on CE/electrolyte/CE structures.

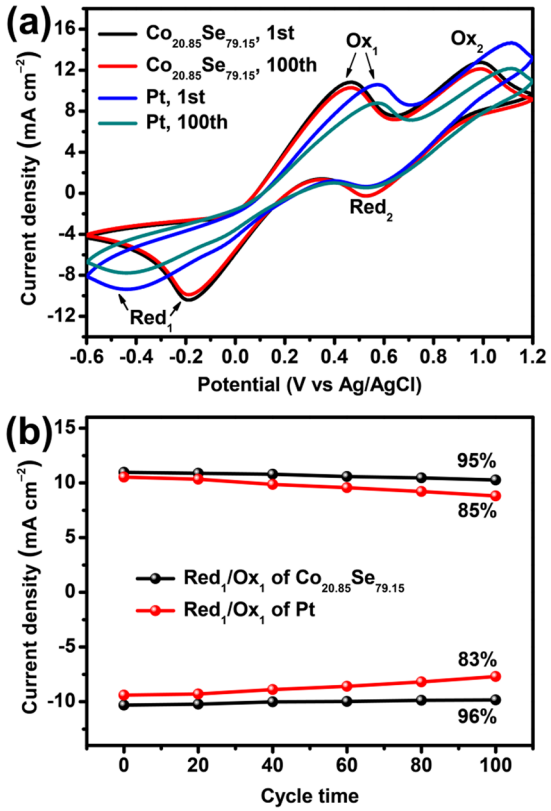

Figure 5. (**a**) 100 cycles of CV plots for $Co_{20.85}Se_{79.15}$ and Pt CEs at 50 mV s^{-1} scan rate in I_3^-/I^- redox electrolyte, (**b**) Changes between cycle number and redox peak current density.

–5.25, –4.94, –5.33, –5.40 and –5.55 eV whereas the corresponding value for the pure Pt electrode is –5.01 eV, respectively. Therefore, the work functions of the $Co_{20.85}Se_{79.15}$ alloy CE show a better match with the potential (–4.90 eV) of the I_3^-/I^- redox electrolyte[18] compared with those of the other CEs, thus resulting in improved electrocatalytic performance. The good match of the $Co_{20.85}Se_{79.15}$ CE work function can be attributed to the ligand effect of the Co and Se transition metals, which would reduce the bond energy between atoms and free electrons[32]. As a result, the electronic configurations of Co and Se atoms near the surface are readjusted in such a way that electrons are prone to participate in the electrolyte (I_3^-) reduction process. Furthermore, the charge transport resistance is defined as the difference between the work function of the CE and the potential of the I_3^-/I^- redox electrolyte of DSSCs[11,33]. For this reason, a lower energy drop would efficiently accelerate the electron transport from electrocatalyst CEs to I_3^-[11,33], which is in good agreement with the above EIS analysis. In this case, the superior electrocatalytic activity of the $Co_{20.85}Se_{79.15}$ CE toward the I_3^- electrolyte can definitely hinder the recombination reaction between I_3^- and excited electrons at the conduction band of nanocrystalline TiO_2, thereby creating an increased photogenerated current density.

Scanning Kelvin Probe Microstructures are also employed to characterize the surface nanostructures of various CEs as shown in Fig. 7(a). Relatively uniform distribution of $Co_{20.85}Se_{79.15}$ alloy CEs was observed, which is in agreement with the SEM. To verify the effect of alloy CEs on the internal transfer kinetics of DSSCs, the Nyquist and Bode phase curves (under light illumination) of DSSCs based on different CEs are displayed in Fig. 7(b,c) and the inset in Fig. 7(b) shows the equivalent circuit where R_{tr} and R_{CE} represent the charge-transfer

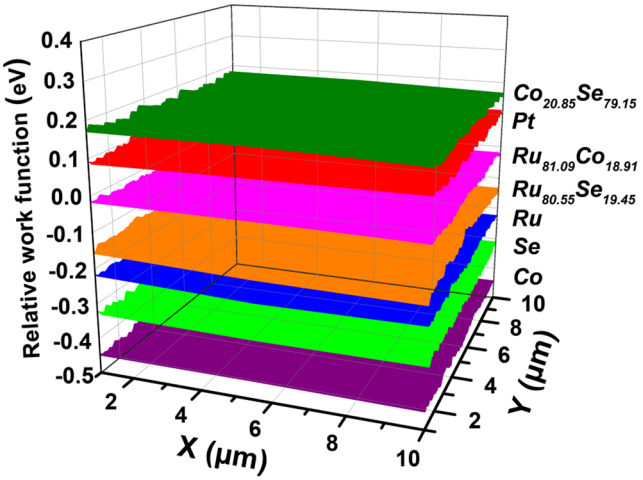

Figure 6. Diagrams of relative work function for various alloy and pristine Pt CEs.

resistances at the dye-sensitized TiO_2/electrolyte interface and electrolyte/CE interfaces for DSSCs, respectively. The electrochemical parameters obtained by fitting the impedance spectra are summarized in Table 5. The DSSC based on the $Co_{20.85}Se_{79.15}$ alloy CE exhibited a lower R_{tr} (3.06 Ω cm^{-2}), suggesting a fast I_3^- to I^- reduction kinetics at the electrolyte/CE interface, where the rapid accumulation of I^- ions can then facilitate their diffusion to the dye-sensitized TiO_2 photoanode/electrolyte interface. Furthermore, the photogenerated electrons in the nanocrystalline TiO_2 photoanode of the $Co_{20.85}Se_{79.15}$ alloy DSSC showed a longer τ_e value compared with those of other devices (Table 5). This result demonstrates that dye molecules are rapidly regenerated by I^- ions, thus enabling fast transport of photogenerated electrons in the mesoporous TiO_2 nanocrystal photoanode, resulting in the superior catalytic activity of the $Co_{20.85}Se_{79.15}$ alloy CE. Furthermore, photovoltaic parameters and synthetic technology comparisons of the various Pt-free transition metal selenides CEs based DSSCs[34–39] were provided as shown in Table 6.

Conclusion

In summary, tunable and Pt-free CEs based on binary alloys ($Ru_{81.09}Co_{18.91}$, $Ru_{80.55}Se_{19.45}$, and $Co_{20.85}Se_{79.15}$) have been synthesized by a simple electrodeposition approach. The results indicate that $Co_{20.85}Se_{79.15}$ alloy CEs possess outstanding electrocatalytic properties towards I_3^- reduction, which can be attributed to their higher number of active sites, reduced interfacial resistance, and matched work function with the I_3^-/I^- redox electrolyte. The $Co_{20.85}Se_{79.15}$ alloy-based CE device displays a higher PCE of 7.08% compared with that of a pure Pt CE (5.80%) as well as preferable stability. Although the obtained alloy composition and performance could be further optimized, the easy synthesis method and hopeful efficiency indicate that electrochemical technologies have significant potential for the development of low-cost, high efficiency and stable DSSCs.

Experimental Section

Synthesis of RuCo/RuSe/CoSe alloy and pristine Pt CEs. The RuCo, RuSe and CoSe alloys were synthesized by electrochemical co-electrodeposition on a cleaned fluorine-doped tin oxide (FTO, sheet resistance 12 Ω sq^{-1}, purchased from Sunlaite) glass substrate, using a galvanostatic approach on the electrochemical workstation. First, a solution (A: 3 mM $RuCl_3$, 2 mM $CoSO_4$; B: 3 mM $RuCl_3$, 2 mM SeO_2; C: 2 mM $CoSO_4$, 3 mM SeO_2) and 100 mM LiCl were dispersed by ultrasonic waves for 30 min. Then, the deposition was carried out in a three-electrode system equipped with an FTO substrate (working electrode), a Pt electrode (counter electrode) and Ag/AgCl (reference electrode). The procedure was performed at a current density of 0.25 mA cm^{-2} for 600 s. Finally, the synthesized alloy CEs were rinsed with deionized water and dried at 80 °C in a vacuum furnace. For comparison, pristine metal CEs were also prepared with a 5 mM $RuCl_3$, 5 mM $CoSO_4$, 5 mM SeO_2 under the same conditions, respectively. The pristine Pt CE was also prepared by cyclic voltammetry in the range of –0.8~0.6 V by using 5 mM H_2PtCl_6 solution, the scan parameter was controlled at 10 mV s^{-1} for 5 cycles.

Electrochemical characterization. A CHI760E electrochemical workstation equipped with a three-electrode device was utilized to assess the electrocatalytic performance of the prepared CEs. Cyclic voltammetry (CV) measurements were carried out in an auxiliary electrolyte consisting of 500 mM $LiClO_4$, 10 mM I_2 and 50 mM LiI in acetonitrile at scan rates of 25, 50, 75, 100 and 125 mV s^{-1}, respectively. Electrochemical impedance spectroscopy (EIS) measurements were performed on symmetrical dummy solar cells with identical CE structures at frequencies ranging from 0.01 to 10^5 Hz and amplitude of 10 mV in air, respectively. Tafel polarization plots were also recorded on symmetrical cells at a scan rate of 10 mV s^{-1}. Then, EIS measurements of the DSSCs were performed with an amplitude of 10 mV, under sunlight illumination.

Fabrication of DSSCs. A TiO_2 nanoparticle film-based on the FTO glass substrate was prepared according to the procedure described in our previous work. Specific as follows: a mixed solution of 20 mL ethanol and

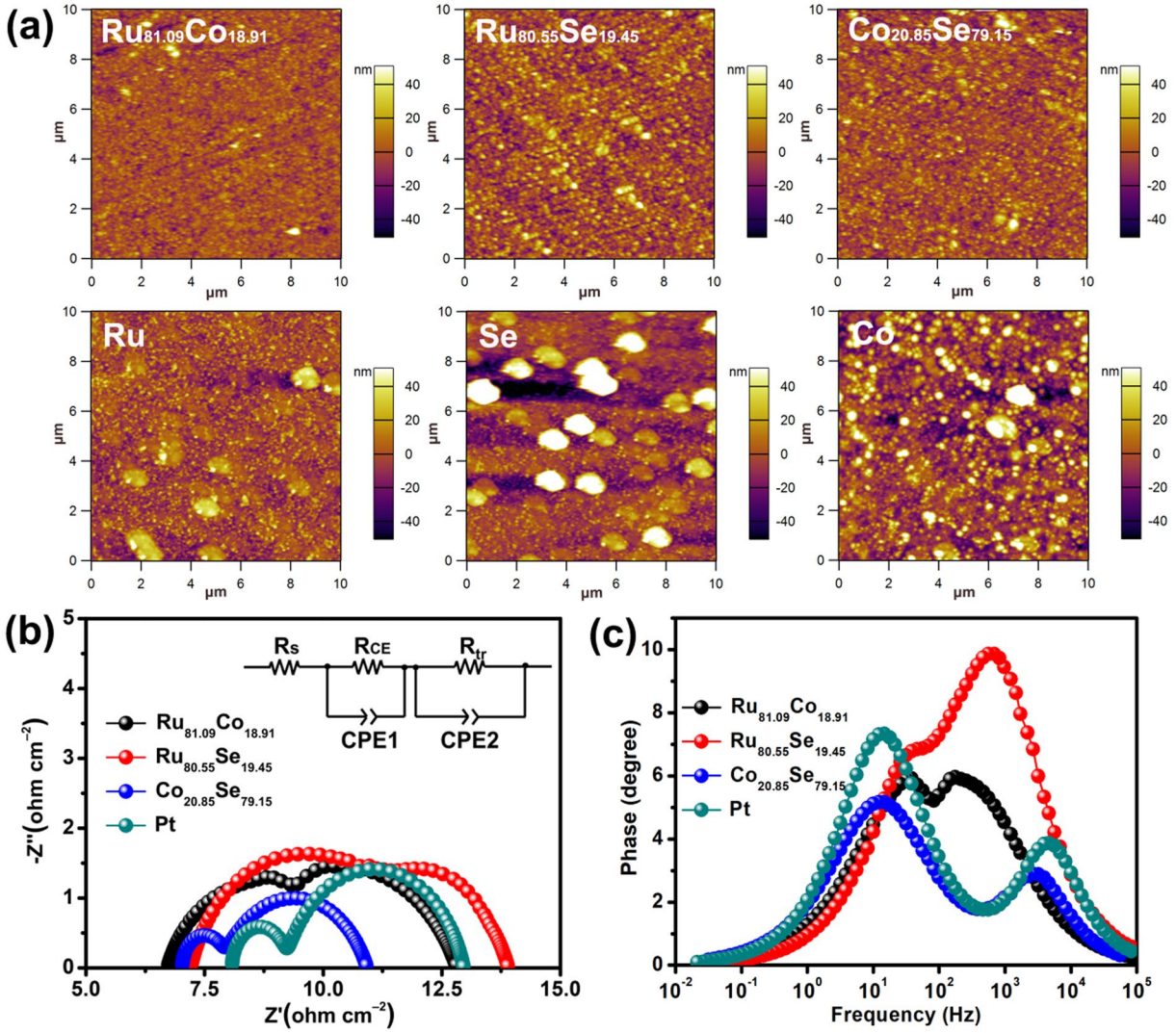

Figure 7. (**a**) Scanning kelvin probe images of different CEs, (**b**) Nyquist EIS plots of the DSSCs with various alloy CEs, and (**c**) Bode phase plots (under sunlight conditions).

Light	R_{CE} (Ω cm^{-2})	R_{tr} (Ω cm^{-2})	f_{peak} (Hz)	τ_e (ms)
$Ru_{81.09}Co_{18.91}$	3.99	3.95	38.31	4.16
$Ru_{80.88}Se_{19.45}$	5.36	4.07	46.42	3.43
$Co_{20.85}Se_{79.15}$	0.84	3.06	12.12	13.14
Pt	1.12	3.78	14.68	10.85

Table 5. Electrochemical parameters obtained from the impedance spectra of various CEs based DSSCs under AM 1.5 G simulated sunlight.

8 mL tetrabutyl titanate was magnetically stirred for 30 min. Then, the acquired solution was added to a solution consisting of 5 mL deionized water and 40 mL acetic acid with magnetic stirring for 2 h. Afterward, the solution underwent a hydrothermal process at 230 °C for 12 h. Finally, the photoanode was obtained after washing the products and spin-coating TiO_2 nanoparticle on FTO glass. The thickness and active area of the photoanode film were controlled to 10 μm and 0.25 cm^2, respectively. Then, the prepared TiO_2 photoanode was sensitized in a 0.50 mM N719 ethanol solution for 18 h. Afterward, the DSSCs were obtained by assembling the dye-sensitized TiO_2 photoanode and CEs with Surlyn tape, followed by injection of the I_3^-/I^- redox electrolyte (0.05 M I_2, 0.1 M LiI, 0.3 M 1,2-dimethyl-3-propylimidazoliumiodide, and 0.5 M tertbutylpyridine).

Photoelectrochemical measurements. The photovoltaic performances of the assembled DSSCs were characterized using a CHI760E electrochemical workstation under simulated solar irradiation with an intensity

CE materials	Method	J_{sc} (mA cm^{-2})	V_{oc} (V)	FF	PCE (%)	PCE Pt (%)	Ref.
$Co_{0.85}Se$	Low-t-hydrothermal	16.74	0.742	0.67	8.30	6.18	[7]
$Ni_{0.85}Se$	Low-t-hydrothermal	16.67	0.740	0.64	7.85	6.18	[7]
$Cu_{0.50}Se$	Low-t-hydrothermal	14.55	0.713	0.62	6.43	6.18	[7]
$Ru_{0.33}Se$	Low-t-hydrothermal	18.93	0.715	0.68	9.22	6.18	[7]
FeSe	Low-t-hydrothermal	17.10	0.733	0.61	7.64	6.18	[7]
$CoSe_2$/N-C@CC	Solution method + selenization	16.39	0.730	0.70	8.40	8.09	[20]
$CoSe_2$/Porous CS	Carbonization + selenization	15.88	0.690	0.69	7.56	7.40	[21]
$Co_{0.85}Se$	Low-t-hydrothermal	16.98	0.738	0.75	9.40	8.64	[22]
$Ni_{0.85}Se$	Low-t-hydrothermal	15.63	0.739	0.72	8.32	8.64	[22]
NiSe-Ni_3Se_2	Solothermal method	16.31	0.750	0.64	7.83	7.28	[25]
$NiSe_2$	Low-t-hydrothermal	15.72	0.660	0.31	3.28	6.11	[34]
$Ni_{0.9}Co_{0.1}Se$	Low-t-hydrothermal	13.46	0.690	0.39	3.68	6.11	[34]
$Ni_{0.5}Co_{0.5}Se$	Low-t-hydrothermal	15.65	0.700	0.54	6.02	6.11	[34]
$CoSe_2$	Low-t-hydrothermal	14.59	0.710	0.55	5.78	6.11	[34]
$CoSe_2$ NRs	High-t-hydrothermal	18.55	0.753	0.73	10.20	8.17	[35]
$Co_{0.5}Se$	Low-t-hydrothermal	13.27	0.721	0.67	6.47	6.18	[36]
$Co_{0.7}Se$	Low-t-hydrothermal	15.36	0.739	0.66	7.46	6.18	[36]
$Co_{0.85}Se$	Low-t-hydrothermal	16.80	0.742	0.67	8.30	6.18	[36]
CoSe	Low-t-hydrothermal	15.47	0.743	0.67	7.75	6.18	[36]
$Co_{1.2}Se$	Low-t-hydrothermal	11.45	0.723	0.65	5.37	6.18	[36]
$Fe_{0.6}Se$	Low-t-hydrothermal	13.95	0.705	0.62	6.08	/	[37]
$Fe_{0.8}Se$	Low-t-hydrothermal	16.75	0.713	0.58	6.87	/	[37]
FeSe	Low-t-hydrothermal	17.72	0.717	0.72	9.16	/	[37]
$Fe_{1.2}Se$	Low-t-hydrothermal	14.56	0.683	0.58	5.77	/	[37]
$NbSe_2$ NSs/C	Chemical + heat treating	15.58	0.770	0.65	7.80	7.90	[38]
$Ni_{0.33}Co_{0.67}Se$ microsphere	Two-step hydrothermal	17.29	0.789	0.67	9.01	8.30	[39]
$Co_{20.85}Se_{79.15}$ nanoparticles	Electrodeposition	15.91	0.710	0.62	7.08	5.80	This work

Table 6. Photovoltaic parameters comparisons of the reported Pt-free transition metal selenides counter electrode based-DSSCs.

of 100 mW cm^{-2} (using a 500 W CHF-XM500 xenon arc lamp as light source). A standard Si solar cell was used to calibrate the intensity of the solar simulator. EIS measurements of the devices were also conducted at frequency ranges of 0.01–10^5 Hz, with a bias voltage and a AC amplitude of 0.68 V and 10 mV, respectively. Results were analyzed by the Z-view software using the corresponding equivalent circuit.

Characterization. The phase structures of the synthesized alloy CEs and pristine metals were characterized by powder X-ray diffraction (XRD, Bruker D8 Advance) with Cu K_α radiation ($\lambda \sim 0.154$ nm) and X-ray photoelectron spectroscopy (XPS, Thermo Fisher Scientific). Field-emission scanning electron microscopy (FESEM, JEOL JSM-6701F, Japan) and energy-dispersive spectroscopy (EDS) measurements were carried out to inspect the microstructures and elemental compositions of the alloy CEs. Scanning Kelvin probe microscopy (SKPM, CH020) was used to determine the relative work functions of the different CEs, with a gold probe serving as a reference electrode (5.1 eV).

Received: 31 December 2019; Accepted: 9 March 2020;
Published online: 08 June 2020

References

1. Peng, Y., Lu, B. Z. & Chen, S. W. Carbon-supported single atom catalysts for electrochemical energy conversion and storage. *Adv. Mater.* **30**, 1801995 (2018).
2. Yang, D. H., Kong, L. J., Zhong, M., Zhu, J. & Bu, X. H. Metal-organic gel-derived Fe_xO_y/nitrogen-doped carbon films for enhanced lithium storage. *Small* **15**, 1804058 (2018).
3. Murakami, T. N. & Koumura, N. Development of next-generation organic-based solar cells: studies on dye-sensitized and perovskite solar cells. *Adv. Energy Mater.* **9**, 1802967 (2018).
4. Li, P. J. & Tang, Q. W. Highly transparent metal selenide counter electrodes for bifacial dye sensitized solar cells. *J. Power Sources* **317**, 43–48 (2016).
5. Wu, M., Lin, X., Hagfeldt, A. & Ma, T. Low-cost molybdenum carbide and tungsten carbide counter electrodes for dye-sensitized solar cells. *Angew. Chem. Int. Ed.* **50**, 3520–3524 (2011).
6. Uppachai, P. *et al.* A substoichiometric tungsten oxide catalyst provides a sustainable and efficient counter electrode for dye-sensitized solar cells. *Electrochimica Acta* **145**, 27–33 (2014).
7. Duan, Y. Y., Tang, Q. W., Liu, J., He, B. L. & Yu, L. M. Transparent metal selenide alloy counter electrodes for high efficiency bifacial dye-sensitized solar cells. *Angew. Chem. Int. Ed.* **53**, 14569–14574 (2014).

8. Liu, T. *et al*. A graphene quantum dot decorated SrRuO3 mesoporous film as an efficient counter electrode for high-performance dye-sensitized solar cells. *J. Mater. Chem. A* **5**, 17848–17855 (2017).
9. Chiang, C. C. *et al*. PtCoFe nanowire cathodes boost short-circuit currents of Ru(II)-based dye-sensitized solar cells to a power conversion effciency of 12.29%. *Adv. Funct. Mater.* **28**, 1703282 (2018).
10. He, B. L. *et al*. Low-cost CoPt alloy counter electrodes for efficient dye-sensitized solar cells. *J. Power Sources.* **260**, 180–185 (2014).
11. Tang, Q. W., Zhang, H. H., Meng, Y. Y., He, B. L. & Yu, L. M. Dissolution engineering of platinum alloy counter electrodes in dye sensitized solar cells. *Angew. Chem.* **127**, 11610–11614 (2015).
12. Calle-Vallejo, F., Koper, M. T. M. & Bandarenka, A. S. Tailoring the catalytic activity of electrodes with monolayer amounts of foreign metals. *Chem. Soc. Rev.* **42**, 5210–5230 (2013).
13. Perera, I. R. *et al*. Application of the tris(acetylacetonato) iron(III)/(II) redox couple in p-type dye-sensitized solar cells. *Angew. Chem. Int. Ed.* **54**, 3758–3762 (2015).
14. Ghouri, Z. K., Elsaid, K., Abdala, A., Abdullah, A. M. & Akhta, M. S. CePd-nanoparticles incorporated carbon nanofibers as efficient counter electrode for DSSCs. *Chemistry Select.* **3**, 12314–12319 (2018).
15. Zou, H. Y., He, B. W., Kuang, P. Y., Yu, J. G. & Fan, K. Ni_xS_y nanowalls/nitrogen-doped graphene foam is an effcient trifunctional catalyst for unassisted artifcial photosynthesis. *Adv. Funct. Mater.* **28**, 1706917 (2018).
16. Li, Y. J., Tang, Q. W., Yu, L. M., Yan, X. F. & Dong, L. Cost-effective platinum alloy counter electrodes for liquid-junction dye-sensitized solar cells. *J. Power Sources* **305**, 217–224 (2016).
17. Cai, H. Y., Tang, Q. W., He, B. L. & Li, P. J. PtRu nanofiber alloy counter electrodes for dye-sensitized solar cells. *J. Power Sources* **258**, 117–121 (2014).
18. Yang, Q. M. *et al*. Ternary platinum alloy counter electrodes for high-efficiency dye-sensitized solar cells. *Electrochim. Acta* **190**, 85–91 (**2016**).
19. Zhang, J. J., Ma, M. M., Tang, Q. W. & Yu, L. M. Multistep electrochemical deposition of hierarchical platinum alloy counter electrodes for dye-sensitized solar cells. *J. Power Sources.* **303**, 243–249 (2016).
20. Lu, W. L., Jiang, R., Yin, X. & Wang, L. Y. Porous N-doped-carbon coated $CoSe_2$ anchored on carbon cloth as 3D photocathode for dye-sensitized solar cell with efficiency and stability outperforming Pt. *Nano Res.* **12**, 159–163 (2019).
21. Li, W. D. *et al*. $CoSe_2$/porous carbon shell composites as high-performance catalysts toward tri-iodide reduction in dye-sensitized solar cells. *Inorg. Chem. Front.* **6**, 2550–2557 (2019).
22. Gong, F., Wang, H., Xu, X., Zhou, G. & Wang, Z. S. *In situ* growth of Co0.85Se and Ni0.85Se on conductive substrates as high-performance counter electrodes for dye-sensitized solar cells. *J. Am. Chem. Soc.* **134**, 10953–10958 (2012).
23. Wei, W. T. *et al*. Partial ion-exchange of nickel-sulfide-derived electrodes for high performance supercapacitors. *Chem. Mater.* **26**, 3418–3426 (2014).
24. Zhang, X., Zhen, M. M., Bai, J. W., Jin, S. W. & Liu, L. Efficient NiSe-Ni_3Se_2/graphene electrocatalyst in dye-sensitized solar cells: the role of hollow hybrid nanostructure. *ACS Appl. Mater. Inter.* **8**, 17187–17193 (2016).
25. Xiong, X. H. *et al*. Controlled synthesis of NiCo2S4 nanostructured arrays on carbon fiber paper for high-performance pseudocapacitors. *Nano Energy*. **16**, 71–80 (2015).
26. Park, E. H., Shin, S. H., Bae, K. H., Dao, V. D. & Choi, H. S. Electrochemical catalytic activity of PtxMo1-x alloy nanoparticles applied to the counter electrode of liquid junction photovoltaic devices. *Sol. Energy.* **153**, 126–133 (2017).
27. Yang, P. Z. & Tang, Q. W. Robust counter electrodes from nanoporous NiM (M= Pt, Pd) alloys for dye-sensitized solar cells. *Electrochim. Acta.* **182**, 827–833 (2015).
28. He, B. L., Tang, Q. W., Zhang, H. H. & Yu, L. M. Counter electrode electrocatalysts from binary Pd-Co alloy nanoparticles for dye-sensitized solar cells. *Sol. Energy.* **124**, 68–75 (2016).
29. Tang, Q. W., Wang, J., He, B. L. & Yang, P. Z. Can dye-sensitized solar cells generate electricity in the dark. *Nano Energy.* **33**, 266–271 (2017).
30. Ma, J., Shen, W. & Yu, F. Graphene-enhanced three-dimensional structures of MoS2 nanosheets as a counter electrode for Pt-free efficient dye-sensitized solar cells. *J. Power Sources* **351**, 58–66 (2017).
31. Liu, W. W., Hong, C. X., Wang, H. G., Zhang, M. & Guo, M. Enhanced photovoltaic performance of fully flexible dye-sensitized solar cells based on the Nb2O5 coated hierarchical TiO2 nanowire-nanosheet arrays. *Appl. Surf. Sci.* **364**, 676–685 (2016).
32. Zhang, S. *et al*. Tuning nanoparticle structure and surface strain for catalysis optimization. *J. Am. Chem. Soc.* **136**, 7734–7739 (2014).
33. Liu, W. W., Wang, H. G., Wang, X. F., Zhang, M. & Guo, M. Titanium mesh supported TiO2 nanowire arrays/Nb-doped TiO2 nanoparticles for fully flexible dye-sensitized solar cells with improved photovoltaic properties. *J. Mater. Chem. C* **4**, 11118–11128 (2016).
34. Theerthagiri, J. *et al*. Synthesis and characterization of $(Ni_{1-x}Co_x)Se_2$ based ternary selenides as electrocatalyst for triiodide reduction in dye-sensitized solar cells. *J. Solid State Chem.* **238**, 113–120 (2016).
35. Sun, H., Zhang, L. & Wang, Z. S. Single-crystal $CoSe_2$ nanorods as an efficient electrocatalyst for dye-sensitized solar cells. *J. Mater. Chem. A* **2**, 16023–16029 (2014).
36. Duan, Y. Y. *et al*. Bifacial dye-sensitized solar cells with transparent cobalt selenide alloy counter electrodes. *J Power Sources* **284**, 349–354 (2015).
37. Liu, J., Tang, Q. W., He, B. L. & Yu, L. M. Cost-effective, transparent iron selenide nanoporous alloy counter electrode for bifacial dye-sensitized solar cell. *J. Power Sources* **282**, 79–86 (2015).
38. Guo, J. H. *et al*. Cost-effective and morphology-controllable niobium diselenides for highly efficient counter electrodes of dye-sensitized solar cells. *J. Mater. Chem. A* **1**, 11874–11879 (2013).
39. Qian, X., Li, H. M., Shao, L., Jiang, X. C. & Hou, L. X. Morphology-tuned synthesis of nickel cobalt selenides as highly efficient Pt-free counter electrode catalysts for dye-sensitized solar cells. *ACS. Appl. Mater. Interfaces* **8**, 29486–29495 (2016).

Acknowledgements

This work was supported by the National Natural Science Foundation of China (No. 51572020) and a project (No. 26-061707) founded by Lanzhou University of Technology. In addition, the research is also supported by the Ministry of Science and Technology through Grant no. 108-2218-E-007-045-, 107-2923-E-007-002-MY3, 107-2218-E-007-055-, 107-2112-M-007 -030-MY3 and 107-3017-F-007-002. Y.L. Chueh greatly appreciates the use of the facility at CNMM.

Author contributions

Y.-L.C. and W.W.L. supervised the research project. W.J. is responsible for the integration of the device. L.B.K., W.W.L., L.L., and Z.M.W. conducted the mechanism study. W.J. and Y.C.L. operated the electrical characterization. W.J.N., M.C.L. and W.J. operated the material characterization.

Competing interests

The authors declare no competing interests.

Additional information

Supplementary information is available for this paper at https://doi.org/10.1038/s41598-020-64965-7.

Correspondence and requests for materials should be addressed to W.-W.L. or Y.-L.C.

Reprints and permissions information is available at www.nature.com/reprints.

Publisher's note Springer Nature remains neutral with regard to jurisdictional claims in published maps and institutional affiliations.